NeuroImage 195 (2019) 48–58

Contents lists available at ScienceDirect

NeuroImage

journal homepage: www.elsevier.com/locate/neuroimage

Ultrafast fMRI of the rodent brain using simultaneous multi-slice EPI

Hsu-Lei Lee [a,b], Zengmin Li [a], Elizabeth J. Coulson [a,c], Kai-Hsiang Chuang [a,b,*]

[a] Queensland Brain Institute, The University of Queensland, Brisbane, Australia
[b] Centre of Advanced Imaging, The University of Queensland, Brisbane, Australia
[c] School of Biomedical Sciences, The University of Queensland, Brisbane, Australia

ARTICLE INFO

Keywords:
Functional MRI
Simultaneous multi-slice
Multi-band
Functional connectivity
Rodent
Temporal resolution

ABSTRACT

Increasing spatial and temporal resolutions of functional MRI (fMRI) measurement has been shown to benefit the study of neural dynamics and functional interaction. However, acceleration of rodent brain fMRI using parallel and simultaneous multi-slice imaging techniques is hampered by the lack of high-density phased-array coils for the small brain. To overcome this limitation, we adapted phase-offset multiplanar and blipped-controlled aliasing echo planar imaging (EPI) to enable simultaneous multi-slice fMRI of the mouse brain using a single loop coil on a 9.4T scanner. Four slice bands of $0.3 \times 0.3 \times 0.5\,mm^3$ resolution can be simultaneously acquired to cover the whole brain at a temporal resolution of 300 ms or the whole cerebrum in 150 ms. Instead of losing signal-to-noise ratio (SNR), both spatial and temporal SNR can be increased due to the increased k-space sampling compared to a standard single-band EPI. Task fMRI using a visual stimulation shows close to 80% increase of z-score and 4 times increase of activated area in the visual cortex using the multiband EPI due to the highly increased temporal samples. Resting-state fMRI shows reliable detection of bilateral connectivity by both single-band and multiband EPI, but no significant difference was found. Without the need of a dedicated hardware, we have demonstrated a practical method that can enable unparallelly fast whole-brain fMRI for preclinical studies. This technique can be used to increase sensitivity, distinguish transient response or acquire high spatiotemporal resolution fMRI.

1. Introduction

Recent advances in ultrahigh field MRI and parallel imaging techniques have shown that increasing spatial and temporal resolutions of functional MRI (fMRI) could benefit the study of neural dynamics and functional interaction. High spatial resolution can improve blood oxygenation level dependent (BOLD) sensitivity by reducing within voxel susceptibility artifacts and partial volume effect (Frahm et al., 1993), and allows resolving hemodynamic responses from individual cortical columns (Duong et al., 2001; Harel et al., 2006) or cortical layers (Siero et al., 2011; Poplawsky et al., 2015; Goense et al., 2016), which may further be used to infer information flow (Huber et al., 2017). Although hemodynamic response is slow, it has been demonstrated that high temporal resolution (>1 Hz) helps not only to increase BOLD sensitivity and statistical power (Neggers et al., 2008; Posse et al., 2012; Smith et al., 2013), to distinguish/reduce physiological noise (Chuang and Chen, 2001; Hennig et al., 2007; Tong et al., 2014), but also allows the detection of high frequency neural activation (Lewis et al., 2016) and resting-state oscillation above the conventional 0.1 Hz range (Boubela et al., 2013; Lee et al., 2013; Lin et al., 2015; Chen and Glover, 2015). As the neural basis of such fast hemodynamic activity is unclear, animal studies are needed to understand its neurophysiological origins (Chuang and Nasrallah, 2017).

Conventionally, high temporal resolution requires the sacrifice of spatial resolution and coverage, or vice versa. In recent years, simultaneous multi-slice (SMS) techniques have emerged which can accelerate data acquisition by exciting several spatially distributed slices simultaneously with multiband composite radiofrequency (RF) pulses and using array coil sensitivity information to resolve aliased and mixed signals from the excited slices. It shortens volume repetition time (TR) by the number of simultaneously excited slices and is particularly beneficial for single-shot sequences such as echo-planar imaging (EPI) whereas conventional 2D parallel imaging approaches (Pruessmann et al., 1999; Griswold et al., 2002) can only reduce the TR partially. The SMS techniques have been widely adopted for high temporal and spatial resolutions in fMRI and diffusion tensor imaging of human brain (Feinberg et al., 2010; Moeller et al., 2010; Feinberg and Yacoub, 2012; Setsompop et al., 2012).

As large number of receiving coils in the accelerated slice direction is required to provide additional spatial information, it is currently difficult

* Corresponding author. Queensland Brain Institute and Centre for Advanced Imaging, The University of Queensland, Brisbane, Queensland, 4072, Australia.
E-mail address: kaichuang@gmail.com (K.-H. Chuang).

https://doi.org/10.1016/j.neuroimage.2019.03.045
Received 18 December 2018; Received in revised form 5 March 2019; Accepted 19 March 2019
Available online 22 March 2019

to apply SMS techniques to rodent fMRI because of the very limited number of receiving coils that can be positioned on the small rat and, particularly, mouse brains. Nonetheless, there are a few SMS techniques that does not rely on multiple receiving coils. Hadamard encoding (Maudsley, 1980; Souza et al., 1988) applies different phase pattern for n simultaneously excited slice in n repetitions, followed by linear combinations of the n images to separate individual slice images. Since it needs more repetitions, it is not useful for single-shot EPI acquisition. Phase-offset multiplanar (POMP; Glover, 1991) technique is another method that only requires 2D Fourier transforms for image reconstruction. POMP uses phase-modulated multiband RF pulses to introduce different phase gradients in k-space for each slice, which shifts each slice image to a different phase-encoding location so the resulted images do not overlap. In order to avoid aliasing of simultaneously excited slices, the field-of-view (FOV) in the phase-encoding direction may have to be extended. However, in single-shot sequences it is not possible to generate phase gradients along phase-encoding direction through RF pulse manipulation. Inspired by blipped-Controlled Aliasing in Parallel Imaging (CAIPI) technique (Setsompop et al., 2012), Lan et al. (2017) proposed a POMP-EPI technique that utilizes slice-select gradient blips to impose different amount of linear phase for different slices between each readout lines. With an extended FOV, each slice will then be shifted to a different portion of the FOV and allows acceleration in slice-select direction and increases fMRI acquisition efficiency in human brain (Lan et al., 2017). Since POMP-EPI increases phase encoding lines to accommodate the simultaneously acquired slices, it can only accelerate few slices before the echo train becomes too long with image quality degraded by susceptibility artifacts. As rodent fMRI is generally acquired at ultrahigh field (≥7T) with significant susceptibility artifacts (Hong et al., 2015), whether it is feasible to acquire SMS with this approach is unclear.

In this study, we further developed and optimized POMP-EPI for ultrafast fMRI of the mouse brain at 9.4T. Taking advantage that rodent brain is like a narrow ellipsoid in the coronal plane, two slices could be acquired simultaneously without increasing a typically square FOV and matrix size. With a moderate increase of phase encoding, a multiband (MB) factor of 4 was achieved with 16 slices covering the whole brain with $0.3 \times 0.3 \times 0.5\,mm^3$ spatial resolution in a TR of 300 ms. Using sequence parameters optimized in phantom, *in vivo* mouse fMRI of visual stimulation and resting state were evaluated. Ultrafast fMRI with TR of 150 ms covering the entire cerebrum was also demonstrated.

2. Methods

2.1. Multiband RF pulse and Multiband-EPI (MB-EPI) sequence

For SMS excitation, multiband RF pulses based on a Hermite pulse was created using the Fourier shift theorem proposed by Müller (1988). The Hermite pulse $\omega_1(t)$ was generated from a product of Hermite polynomials and a Gaussian function which has the form of

$$\omega_1(t) = \left[1 - \left(\frac{t}{T}\right)^2\right] e^{-\left(\frac{t}{T}\right)^2}$$

where T is a constant that determines the pulse width.

Fig. 1 shows the 4-band MB-EPI slice acquisition scheme. A 4-band RF pulse was used to excite slices that are 0.5 mm thick and 2.4 mm apart (Fig. 1a) to cover an FOV of 9.6 mm in the slice-select direction. During EPI acquisition, slice-select gradient blips were applied between the readout lines (Fig. 1c) to introduce slice-dependent linear phase increments along k_y direction and create a k-space pattern which cycles every four readout lines, as shown in Fig. 1b. The amplitude of the blipped gradient was selected so that the phase difference of successive simultaneously excited slices was exactly $\pi/2$. It effectively shifts the acquired slices FOV/4 apart from each other, so the aliasing can be avoided with increased FOV (Setsompop et al., 2012; Lan et al., 2017).

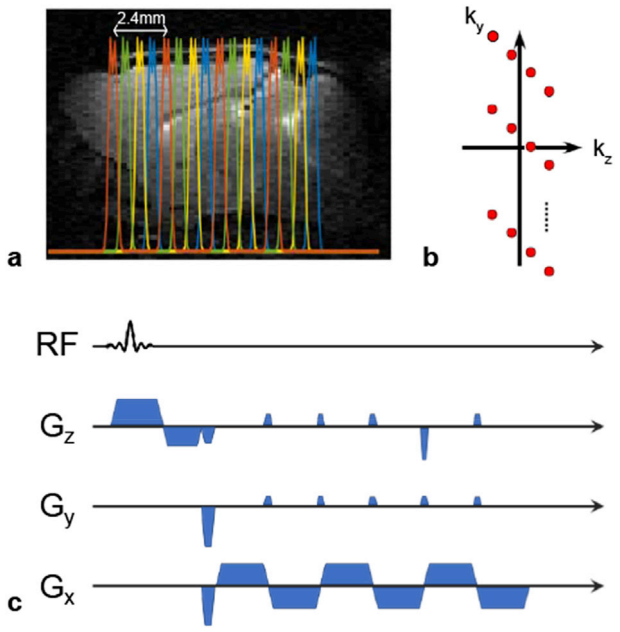

Fig. 1. Multiband EPI pulse sequence. a) Multiband excitation slice profiles using a four-band Hermite RF pulse. Slices of the same color were excited simultaneously. Each volume contains 4 excitations (16 slices in total) to acquire a whole brain. **b)** The locations of acquired k_y and k_z lines. For MB = 4 scans, four k-space lines form a cycle in the k_y-k_z direction, so the individual slice image is shifted for FOV/4 after reconstruction. **c)** Pulse sequence diagram of MB-EPI. G_z gradient blips between the readout lines induce an extra phase shift between each phase-encoding line to create the acquisition pattern shown in b).

During image reconstruction, the extra dephasing induced by the G_z blips is compensated by adding slice-dependent phase terms to each k-space line, which refocuses the simultaneously excited slices at different location along the phase encoding direction and removes the ghost images. As adding G_z blips to the single-band EPI (SB-EPI) acquisition also induces through-slice dephasing (Setsompop et al., 2012), residual ghosting could appear at FOV/MB locations. We also measured the ghosting artifact level in the 4-band MB-EPI protocols and compared with the SB-EPI using the same extended FOV and phase encoding.

2.2. Phantom preparation

A cylindrical structural phantom of 17 mm diameter filled with agarose gel (2% w/v in the outer tube) was used for assessing image quality. Inner tube was filled with 4% w/v agarose gel to simulate tissue contrast variations. Different structure patterns along the z direction were created using a 3D printer to differentiate the simultaneously acquired slices.

2.3. Animal preparation

Animal experiments were approved by the animal ethic committee of the University of Queensland and conducted in compliance with the Queensland Animal Care and Protection Act 2001 and the current National Health and Medical Research Council Australian Code of Practice for the Care and Use of Animals for Scientific Purposes. C57BL/6 mice (N = 8, male, age = 10–16 weeks old) were used in the experiments. Mice were anesthetized with 3% isoflurane in a mixture of O_2 and Air in a 1:2 ratio. After inserting an intraperitoneal catheter, the animal was secured on an MRI holder with ear and tooth bars to minimize head motion. A bolus of 0.05 mg/kg medetomidine (Troy Laboratories, Australia) was then injected. 10 min after the bolus injection, constant infusion of 0.1 mg/kg/h medetomidine (i.p.) was started to maintain the sedative level and the isoflurane level was reduced to 0.25–0.5%. The respiration

rate and rectal temperature were continuously monitored (Model 1030, SAII, USA), with the temperature maintained at 36.5–37 °C by a water heater. The peripheral oxygen saturation (SpO_2) and heart rate were monitored by a pulse oximeter (SAII).

2.4. Stimulation design

For visual stimulation, an optical fiber was attached to the MRI holder, pointed to a light diffuser and connected to a light-emitting diode blue light source (Model M470F3, Thorlabs, USA) which was controlled by a data acquisition device (USB-3101, Measurement Computing, USA) and an in-house program running on Matlab (The MathWorks Inc., USA). Stimulation was done in a block design with alternating 39 s resting and 21 s stimulation, repeated 3 times and adding another 60 s of resting at the end (total duration 4 min). Visual stimulation was done by flashing blue light (470 nm, 0.1 mW output power at the end of a single optical fiber) inside the scanner bore with 20 ms duration at 5 Hz.

2.5. MRI acquisition

MRI was conducted on a on a 9.4T pre-clinical scanner (Biospec 9.4/30, AVIII HD, PV6.0.1, Bruker BioSpin MRI GmbH, Ettlingen, Germany) with a gradient insert (model BGA-12S HP, Bruker) of max amplitude = 440 mT/m and slew rate 3440 T/m/s. A 23 mm volume transmit/receive coil (Bruker) was used for the phantom test and an 86 mm volume transmit coil with a 10 mm single-channel receiving surface coil (Bruker) were used for *in vivo* imaging. Localized high-order shim (MAPshim) based on B_0 map was applied. High resolution structural MRI was acquired using fast spin echo with TR/TE = 5500/40 ms.

For phantom imaging, a conventional single-shot gradient-echo SB-EPI with 20 and 16 single-slice excitations per TR, where slice thickness was 0.5 mm with 0.1 mm gaps, in-plane resolution = $0.3 \times 0.3\ mm^2$ (FOV = $19.2 \times 19.2\ mm^2$ with matrix size = 64×64) and bandwidth = 300 kHz, was used as the reference standard. Flip angles were chosen as the Ernst angle for gray matter T_1 at 9.4T which is around 2000 ms (de Graaf et al., 2006). Time-series were acquired at TR = 1000 ms and flip angle = 52° for 4 min (240 repetitions) after 10 s of dummy cycles. Two echo time (TE) values (17.7 and 15 ms) were compared to two MB-EPI sequences (see details below). Saturation slice was applied to null out half of the FOV in phantom to only acquire signal with a dimension similar to the mouse brain. The 4-band MB-EPI sequence had an extended FOV of 38.4 mm and the phase encoding step was increased to 128 to maintain the same in-plane resolution ($0.3 \times 0.3\ mm^2$) as SB-EPI. This increased phase-encoding number increased the minimum TE to 17.7 ms for full k-space acquisition (matrix size = 64×128). To reduce susceptibility effects of the prolonged echo train, ¾ partial Fourier (matrix size = 64×96) and shorter TE of 15 ms were used in the second MB-EPI protocol. Due to the gradient duty cycle limit, the achievable acceleration was less than four-fold which allowed the TR to be reduced to 300 ms while keeping other parameters unchanged. To test the effect of G_z blips on image quality, images were acquired using 4-band MB-EPI gradient scheme but with single-band RF pulse, and compared with regular SB-EPI results. Key sequence parameters for phantom tests were listed in Table 1. All phantom experiments were repeated three times to ensure consistency of the assessment.

Based on the phantom tests, the MB-EPI with partial Fourier acquisition was chosen for *in vivo* study. Eight mice were scanned using 4 sets of sequence parameters listed in Table 2. SB-EPI and MB-EPI of the same nominal spatial resolution and coverage (16 slices) were scanned with TE = 15 ms, and with TR of 1000 ms (flip angle = 52°) and 300 ms (flip angle = 30°), respectively. A MB-EPI of TR/TE = 300/11 ms for further reducing susceptibility artifact was also evaluated. Ultrafast MB-EPI (TR/TE = 150/15 ms, flip angle = 22°) was scanned with reduced spatial coverage (slice number = 12, MB factor = 4), which was sufficient to cover the entire cerebrum. Starting at 45–50 min after the medetomidine bolus injection, fMRI with visual task was conducted for 4 min and repeated for each sequence protocol. Afterward, 10 min long resting-state fMRI scans were acquired using each protocol. To minimize the influence of physiological variation over time, the order of the 4 sequence protocols was pseudo-randomized.

2.6. Assessment of point spread function and T_2* weighting

The point spread function (PSF) of each acquisition scheme used in the *in vivo* imaging was simulated. The k-space weighting function for gray matter tissue of T_2* = 15/25/35/45 ms covering the T_2* range from 7.0 T to 16.4T (Guilfoyle et al., 2003; de Graaf et al., 2006; Pohmann et al., 2011) was simulated in the phase-encoding direction and Fourier transformed to obtain the PSF. The amount of blurring was defined as the voxel PSF full width at half maximum (FWHM) ratio between two sequences. To evaluate the additional T_2* weighting induced by the increased echo train length, the Tw*-weighted (BOLD) signal intensity of each acquisition scheme was defined as the area under the PSF at the central voxel. The activation signal change was then simulated as the signal intensity variation when T_2* was increased by 0.1 ms over a range of basal T_2* from 15 to 45 ms.

2.7. Data processing

Data were processed with Matlab, FSL (v5.0.11, https://www.fmrib.ox.ac.uk/fsl), AFNI (ver 17.2.05, National Institutes of Health, USA), and ANTs (v2.3.1, http://stnava.github.io/ANTs/). The k-space data of the SMS images were first phase-corrected and reconstructed in Matlab, then cropped and rearranged into proper 3D volumes for further analysis. Motion correction was applied to *in vivo* data using FSL mcflirt. Task fMRI time-series were then high-pass filtered at 0.01 Hz. For resting-state fMRI data, nuisance which includes quadratic drift, 6 motion parameters, and the top 10 principal components of signals outside the brain, was regressed out (Chuang et al., 2019>) and then band-pass filtered (AFNI 3dTproject) to remove signal variations beyond 0.01–0.3 Hz. To evaluate the influence of high frequency component, the resting fMRI data were also analyzed with only highpass filtered at 0.01 Hz. Spatial smoothing by a 0.3 mm Gaussian kernel was applied to both task and resting fMRI.

Brain masks for the *in vivo* time-series were automatically created by PCNN3D (Chou et al., 2011; https://sites.google.com/site/chuanglab/so

Table 1
Sequence parameters of phantom imaging. PF: Partial Fourier.

Sequence	TR (ms)	TE (ms)	FOV (mm^2)	Acquisition Matrix	Slice Number	MB	Flip Angle	Minimum TR (ms)	Minimum TE (ms)
SB-EPI	1000	17.7 15.0	19.2 × 19.2	64 × 64	20	–	52°	625	10.9
MB-EPI	1000 300	17.7 17.7	19.2 × 38.4	64 × 128	20	4	52° 30°	240	17.7
PF-MB-EPI	1000 300	15.0 15.0	19.2 × 38.4	64 × 96	20	4	52° 30°	205	10.8

NOTE: the minimum TR was determined assuming minimum TE was used, and only gradient timing but not duty cycle limit was considered. In a prolonged scan the gradient duty cycle could become too high with minimum TR values and cause instability of the system.

Table 2
Sequence parameters of *in vivo* imaging. PF: Partial Fourier.

Sequence	TR (ms)	TE (ms)	FOV (mm^2)	Acquisition Matrix	Slice Number	MB	Flip Angle	Minimum TR (ms)	Minimum TE (ms)
SB-EPI	1000	15	19.2 × 19.2	64 × 64	16	–	52°	505	10.8
PF-MB-EPI	300	15	19.2 × 38.4	64 × 96	16	4	30°	170	10.8
PF-MB-EPI	150	15	19.2 × 38.4	64 × 96	12	4	22°	135	10.8
PF-MB-EPI	300	11	19.2 × 38.4	64 × 96	16	4	30°	170	10.8

NOTE: the minimum TR was determined assuming minimum TE was used, and only gradient timing but not duty cycle limit was considered.

ftware/3d-pcnn) using motion corrected images and then manually inspected and edited. A study-specific EPI template was generated from the SB-EPI datasets of all mice by nonlinear warping (ANTs) the extracted and B_1 corrected (N4, implemented in ANTs) brain EPI to a 0.2 mm T_2-weighted MRI AMBMC (The Australian Mouse Brain Mapping Consortium) template (Ullmann et al., 2013; http://imaging.org.au/AMBMC/AMBMC). Then all the warped EPI data was intensity normalized and averaged to form the EPI template. Afterward, 2nd pass of nonlinear warping to the EPI template was calculated and applied to the fMRI data.

Spatial Signal-to-Noise Ratio (SNR) was measured as the division of average intensity over the voxels containing 2% agarose gel in phantom or the voxels within the brain mask in *in vivo* images by the standard deviation of intensity in an artifact-free area outside the object (8000 voxels for phantom, 6100 voxels for *in vivo* images). Temporal SNR (tSNR) was calculated voxel-wise inside the whole phantom or whole brain by dividing the temporal mean by the temporal standard deviation of each voxel. The intensity of masked four-band images was first matched to the single-band ones by linear least squares fitting. The percentage difference is then calculated as the residuals divided by the average of the two images. Signal drift was estimated as the average slope of a linear fitting to mean value normalized voxel time-course of the EPI.

2.8. Statistical analysis

For the analysis of task fMRI time-series, a design matrix was created which includes a boxcar waveform convolved by a double gamma function of 2 s initial delay, its first-order temporal derivative, and the 6 estimated motion. Voxel-wise noise autocorrelation was estimated in the residuals and the time-series was pre-whitened accordingly using FSL FILM. 1st-level general linear model (GLM) analysis was conducted for each subject's pre-whitened data to generate individual *z*-maps. After warping the statistical maps to the EPI template, second level random effect analysis was conducted using one-sample *t*-test to find the group activated region ($p < 0.05$, false discovery rate (FDR) corrected). The difference in detection sensitivity between SB-EPI and MB-EPI were compared using repeated measures ANOVA (Prism, GraphPad Software Inc, USA) for mean z-score of all voxels, mean z-score of activated voxels, percentage BOLD signal change, and activated area size in the primary visual cortex (V1). This region of interest (ROI) was created by manually editing the V1 area in the AMBMC atlas to remove mis-matched voxels at the edge of the EPI template. Percentage signal change in a voxel was defined as the beta estimate corresponding to the normalized hemodynamic response function (HRF) regressor in the GLM analysis.

To measure functional connectivity from the resting-state fMRI data, seed-based correlation analysis was performed with seed time-courses defined as the averaged signals from each labeled brain area in the AMBMC atlas. The connectivity was assessed with 4 ROIs, with two from the cortex, V1 and the primary somatosensory (S1) cortices, and two from the subcortical areas, the hippocampus and amygdala. The ROIs were divided into the left and right side. Pearson's correlation coefficients between each voxel and seed time-courses were calculated to generate the functional connectivity map. The correlation of ROI time courses between the hemispheres was calculated as the connectivity strength. Fisher's *z*-transformation was used to convert correlation coefficients to *z* values. Second level random effect analysis was then conducted on the individual *z*-maps using one-sample *t*-test and thresholded at $p < 0.005$, FDR corrected. The difference in connectivity strength detected by SB-EPI and MB-EPI were compared using ANOVA.

3. Results

3.1. Image quality optimization in phantom

Phantom images acquired with single- and four-band EPI over 16 slices are shown in Fig. 2a. In general, both sequences generated good quality images with minimal artifacts. Discrepancy between multiband and single-band acquisitions could be found in areas with strong susceptibility changes and the edge of the object. There was mismatch at the edge between single-band and multiband images with long TE (17.7 ms) and full k-space acquisition (upper row in Fig. 2a). Distortion and blurring due to the prolonged acquisition window of full k-space multiband sequence was largely reduced with short TE (15 ms) and ¾ partial Fourier acquisition (lower row in Fig. 2a). This can be seen in the percentage difference single- and multi-band scans where short TE acquisition produced comparable signal across regions with susceptibility signal drop. Fig. 2c shows the line profiles across a region that has susceptibility induced signal dropout. The mean square error between single- and four-band images is 10.93% ± 1.39% (mean ± standard deviation (STD)) at TE = 17.7 ms, and 9.99% ± 2.86% at TE = 15 ms.

Unlike typical SMS acquisition in human which has certain SNR penalty, the temporal SNR of the four-band EPI were increased whereas the spatial SNR was comparable (Fig. 2b). The four-band acquisition generated 42% ± 4.8% higher tSNR at TR/TE = 1000/17.7 ms, and 59% ± 3.4% higher tSNR at TR/TE = 1000/15 ms when comparing to SB-EPI with the same TR/TE and nominal spatial resolution. Such tSNR advantage would allow shortening TR without much tSNR decrease. When the TR of four-band full k-space acquisition was shortened to 300 ms, tSNR dropped to be 80% ± 3.4% of the SB-EPI with TR/TE = 1000/17.7 ms due to less T1 recovery. With partial Fourier and short TE, the tSNR was 90% ± 4.2% of the SB-EPI.

As the MB-EPI requires higher gradient duty cycle and RF power, it may lead to more system heating and instability. To evaluate the stability of the SMS acquisition, the amount of signal drift was compared between sequences with the same TE during a 3-min scan. For TE = 17.7 ms, SB-EPI had 0.73% ± 0.39% of signal drift, and MB-EPI had 0.46% ± 0.16% (TR = 1000 ms) and 1.42% ± 0.36% (TR = 300 ms). For TE = 15 ms, the signal drift of SB-EPI was 0.85% ± 0.45%, whereas the drift in MB-EPI was 0.34% ± 0.10% (TR = 1000 ms) and 0.81% ± 0.17% (TR = 300 ms). With partial Fourier and short TE, MB-EPI has signal drift comparable to SB-EPI (TR = 1000 ms) at a much short TR of 300 ms.

Table 3 lists the FWHM of the voxel PSF in the phase-encoding direction, estimated for the EPI encoding schemes used in our *in vivo* imaging. For a tissue $T_2^* = 35$ ms (roughly equivalent to the average gray matter tissue T_2^* at 9.4T, Zhao et al., 2004), MB-EPI with ¾ partial Fourier has a 36% increase in the PSF FWHM compared to the regular SB-EPI with the same nominal in-plane resolution of 0.3 mm.

To assess the potentially enhanced T_2^* weighting due to the longer echo train, the activated BOLD signal change as a function of T_2^* was simulated (Supplementary Fig. S1). The MB-EPI (TE = 15 ms, ¾ partial Fourier) generates a percentage signal change that is 10%–20% larger than SB-EPI of the same TE with T_2^* in the range of 15–45 ms. This makes the MB-EPI having an equivalent T_2^* weighting as the SB-EPI with

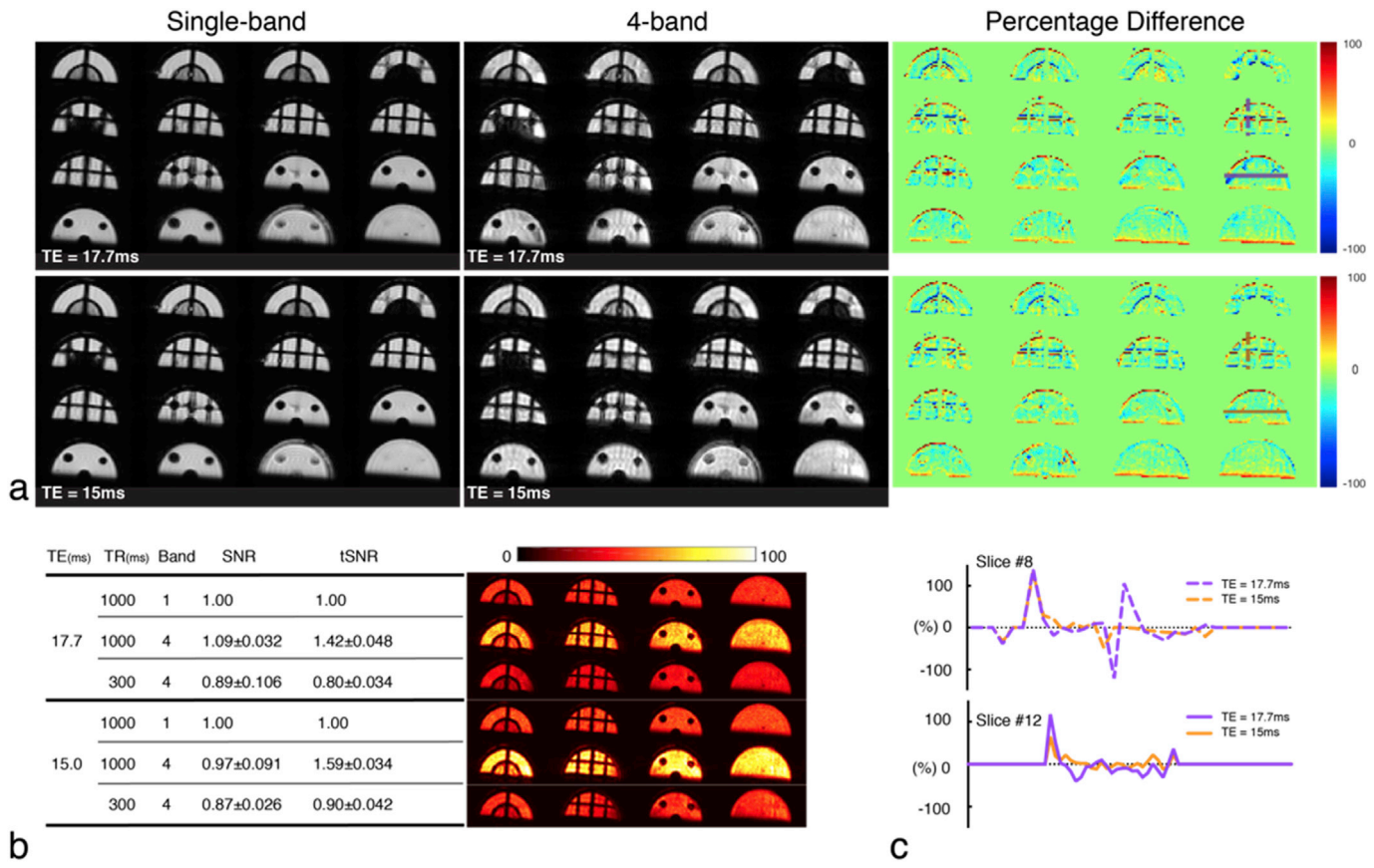

Fig. 2. Image quality in phantom. a) The 1st row shows the single-band (left) and 4-band EPI (center) acquired with TR/TE = 1000/17.7 ms. The 2nd row shows those acquired with TR/TE = 1000/15 ms and ¾ partial Fourier. The percentage difference of the single- and multi-band images is shown in the right. The longer acquisition window of the MB-EPI sequence results in more signal decay and distortion which is prominent at the edge of the phantom object. **b)** SNR and tSNR of the six different protocols used in phantom tests. The tSNR maps on the right show increased tSNR of the MB-EPI. **c)** The line profiles of MB-EPI corresponding to the purple/orange lines in the percentage difference maps show reduced artifacts by partial Fourier and shorter TE.

Table 3
Simulated point spread function. The simulated full width at half maximum (FWHM) of the voxel point spread function in phase-encoding direction of different sequences listed in Table 2, estimated for tissue T_2^* = 15–45 ms. PF: Partial Fourier.

Sequence	SB-EPI	PF-MB-EPI
Nominal Resolution (mm)	0.30	0.30
FWHM (mm) (T_2^* = 45 ms)	0.36	0.49
FWHM (mm) (T_2^* = 35 ms)	0.36	0.49
FWHM (mm) (T_2^* = 25 ms)	0.37	0.50
FWHM (mm) (T_2^* = 15 ms)	0.37	0.52

TE = 17.5 ms.

3.2. Image quality in vivo

Fig. 3 shows example slices of *in vivo* SB- and MB-EPI images and the corresponding tSNR maps from one representative animal. General image quality was comparable to the SB-EPI but more geometric distortion and resolution blurring could be observed in the MB-EPI. Over the whole brain, the tSNR of MB-EPI was 97% ± 19.1% (N = 3) for TR = 300 ms and 65% ± 14.7% for TR = 150 ms compared to the SB-EPI acquired with 1000 ms TR (tSNR = 48.1 ± 9.61). In the visual cortex, the tSNR of MB-EPI was 86% ± 6.8% (N = 8) for TR = 300 ms and 62% ± 3.7% for TR = 150 ms compared to the SB-EPI acquired with 1000 ms TR (tSNR = 76.4 ± 7.62). The tSNR inside the mouse brain decreases with the increasing distance to the 10 mm receiving coil. The

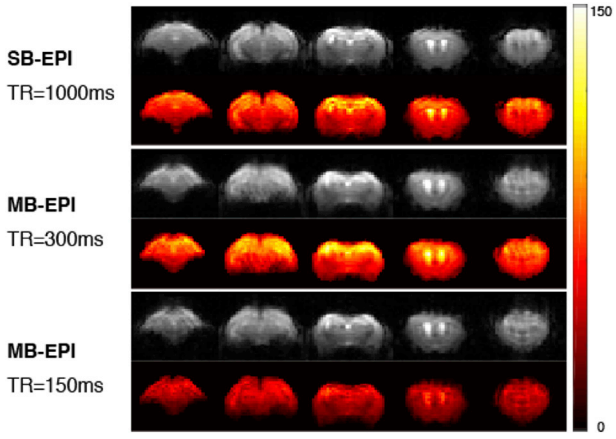

Fig. 3. Image quality of the mouse brain *in vivo*. The EPI magnitude images (gray scale) and tSNR maps (hot color) for SB-EPI with 1000 ms TR (top) and 4-band MB-EPI with 300 ms (middle) and 150 ms TR (bottom). Slight blurring could be seen in the y direction of MB-EPI due to the broadening of the point spread function.

SB-EPI tSNR maps showed that at the location 3 mm deep under the top brain surface the average tSNR dropped to ~62% of the voxels at the top of the brain, and further down to ~49% at the depth of 4.5 mm. The signal drift over the whole brain during a 10-min scan was 2.95% ± 1.40% for SB-EPI, 1.41% ± 0.59% for MB-EPI of TR = 300 ms

and 1.59% ± 0.30% for MB-EPI of TR = 150 ms. There was also insignificant difference in the total displacement estimated by FSL mcflirt which were 0.15 ± 0.187 voxels for SB-EPI, 0.2 ± 0.115 voxels for MB-EPI of TR = 300 ms and 0.32 ± 0.107 for MB-EPI of TR = 150 ms. These together indicate good stability of the MB-EPI protocols using standard hardware available despite a trend of increasing displacement with shorter TR likely due to frequency drift induced by the system heating.

Although this MB-EPI method avoided brain image overlap, it would still suffer from slice aliasing due to the Nyquist ghost artifacts. Ghosting artifacts in MB-EPI caused by the G_z blips are shown in the Supplementary Fig. S2. Without G_z blips, the Nyquist ghost artifact of SB-EPI in the extended FOV and phase encoding scheme could be seen at the ½ FOV. Adding G_z blips to the SB-EPI acquisition caused additional ghost to appear at every ¼ FOV. The average intensity of the ghost at ½ FOV was increased from 3.4% ± 0.22% to 4.4% ± 0.51% (N = 3) of the true object (Fig. S2a), whereas the additional ghosts at ¼ and ¾ FOV had intensity about 1.5% ± 0.69% of the true object. Therefore the reconstructed slice from a MB-EPI would have ghost contamination from the other 3 slices by a factor of around 5.5% ± 0.56% (Fig. S2b).

3.3. Task fMRI

Animal physiology was maintained stable during the fMRI scans with respiration rate = 128 ± 15 breaths/minute, heart rate = 255 ± 40 beats/min, spO_2 = 98% ± 2%, temperature = 36.7 ± 0.3 °C. Fig. 4 shows the visual activation measured by SB-EPI and 3 kinds of 4-band MB-EPI protocols: TR/TE = 300/15 ms, TR/TE = 150/15 ms and TR/TE = 300/11 ms. The increased temporal sampling of the MB-EPI protocols drastically increases the detected activation in the visual cortex and thalamus (Fig. 4a). The average percentage signal change in V1 was higher in the MB-EPI (0.27% ± 0.044%) than that in the SB-EPI (0.22% ± 0.060%) of the same TE (15 ms) but the difference was not statistically significant (Fig. 4d). The signal change was clearly reduced at a shortened TE = 11 ms. The activated area in the V1 was significantly increased by

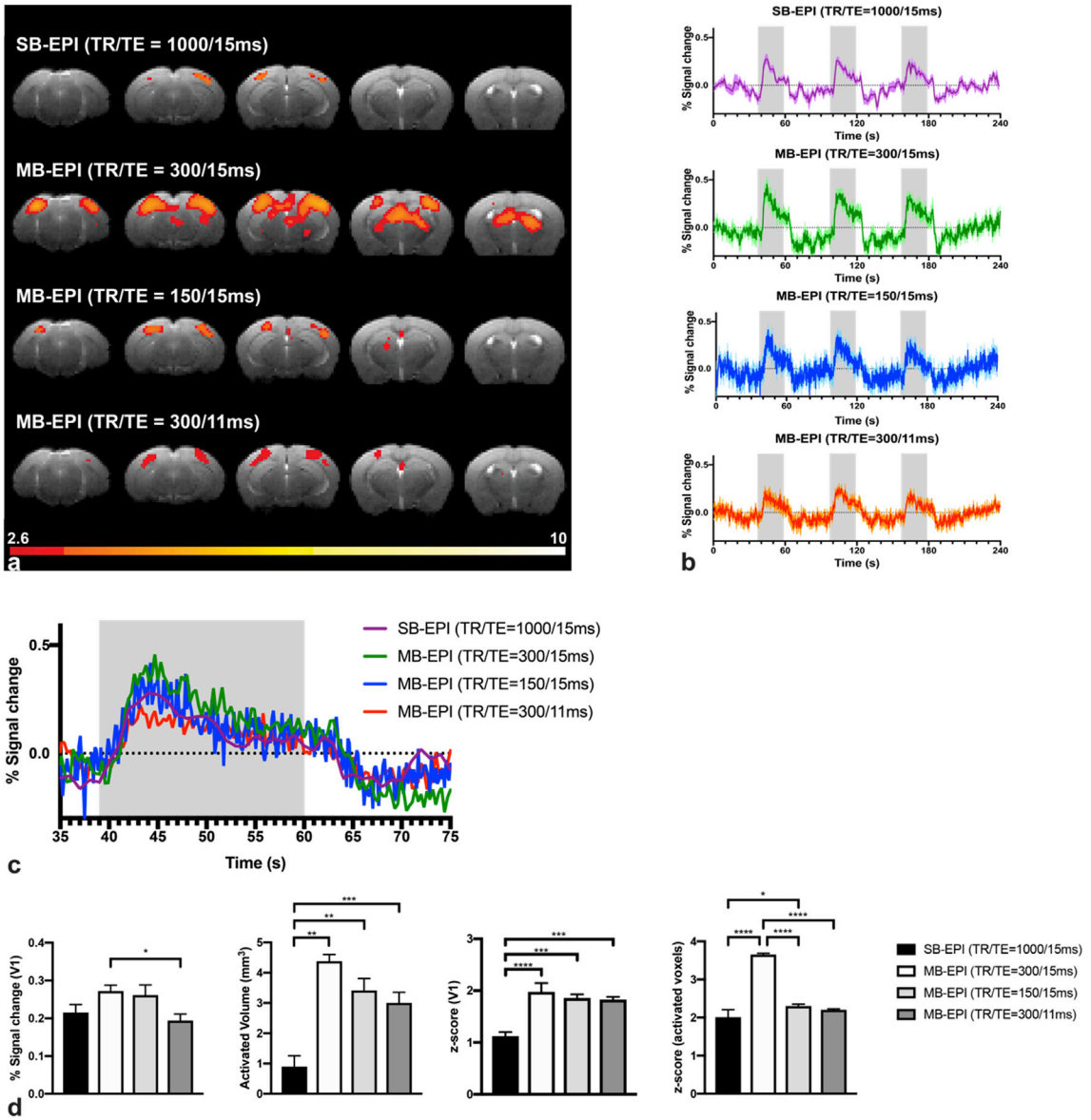

Fig. 4. Visual fMRI. a) Group t-maps ($p < 0.05$, FDR corrected, N = 8) of the 4 sequence protocols, overlaid on a T_2-weighted anatomical image. **b)** Detrended mean BOLD signal averaged across V1 (N = 8). The gray bars indicate the stimulation durations. The shaded color represents the standard error of mean. **c)** The BOLD responses of the first stimulation block. **d)** Comparison of the 4 protocols for percent signal change, activated area, and z-scores of all voxels and activated voxels in V1 (from left to right). *: $p < 0.05$, **: $p < 0.01$, ***: $p < 0.001$, ****: $p < 0.0001$.

more than 4 folds with TR/TE = 300/15 ms and 3 folds with shorter TR or TE due to the significantly increased z-score by about 77% using the MB-EPI (Fig. 4d).

3.4. Resting-state fMRI

Fig. 5 shows the functional connectivity maps and bilateral connectivity strengths measured in 4 seed areas. Unlike the significant increase in the task fMRI, similar spatial extent of the resting-state networks was obtained by SB-EPI and the 3 MB-EPI protocols. More connectivity was detected in the contralateral side and the striatum of the amygdala network using MB-EPI with TR/TE = 300/15 ms, indicating the advantage of increased statistic power for regions with very low SNR like amygdala. However, the connectivity strength was not significantly different (Fig. 5b). To evaluate the influence of high-frequency component, the data was also processed with highpass filtering at 0.01 Hz (Fig. 6). Without the lowpass filter, the group connectivity z-score was generally reduced due to higher noise that includes physiological artifacts. Comparable connectivity maps could be obtained with a lower threshold at $p < 0.05$ (FDR corrected).

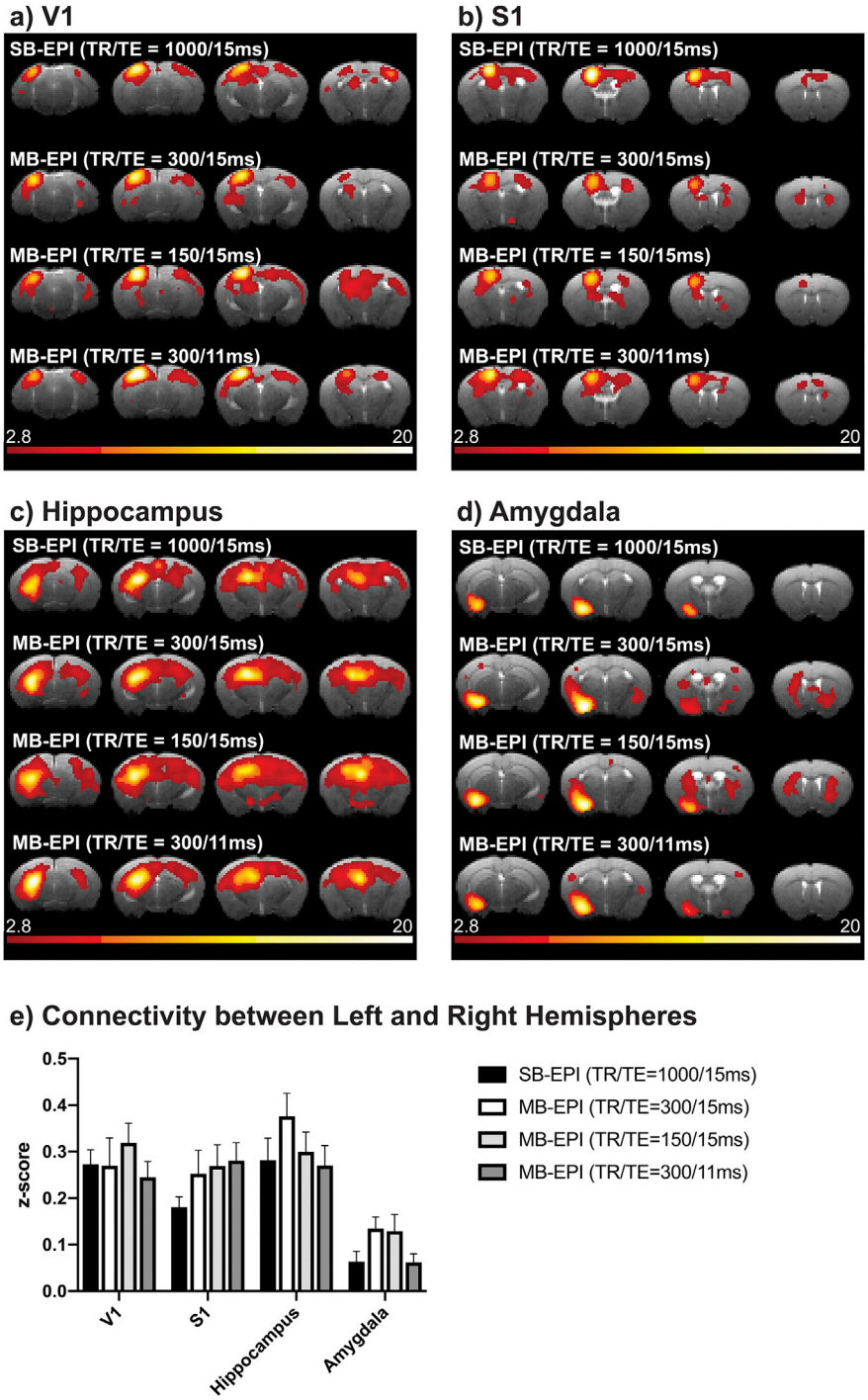

Fig. 5. Resting-state functional connectivity with bandpass filtered at 0.01 and 0.3Hz. Group resting-state functional connectivity maps ($p < 0.005$, FDR corrected, N = 8) using seed regions in the right **a)** V1, **b)** S1, **c)** hippocampus, and **d)** amygdala. **e)** The connectivity strength (z-score) between the left and right seed regions. No significant difference was found.

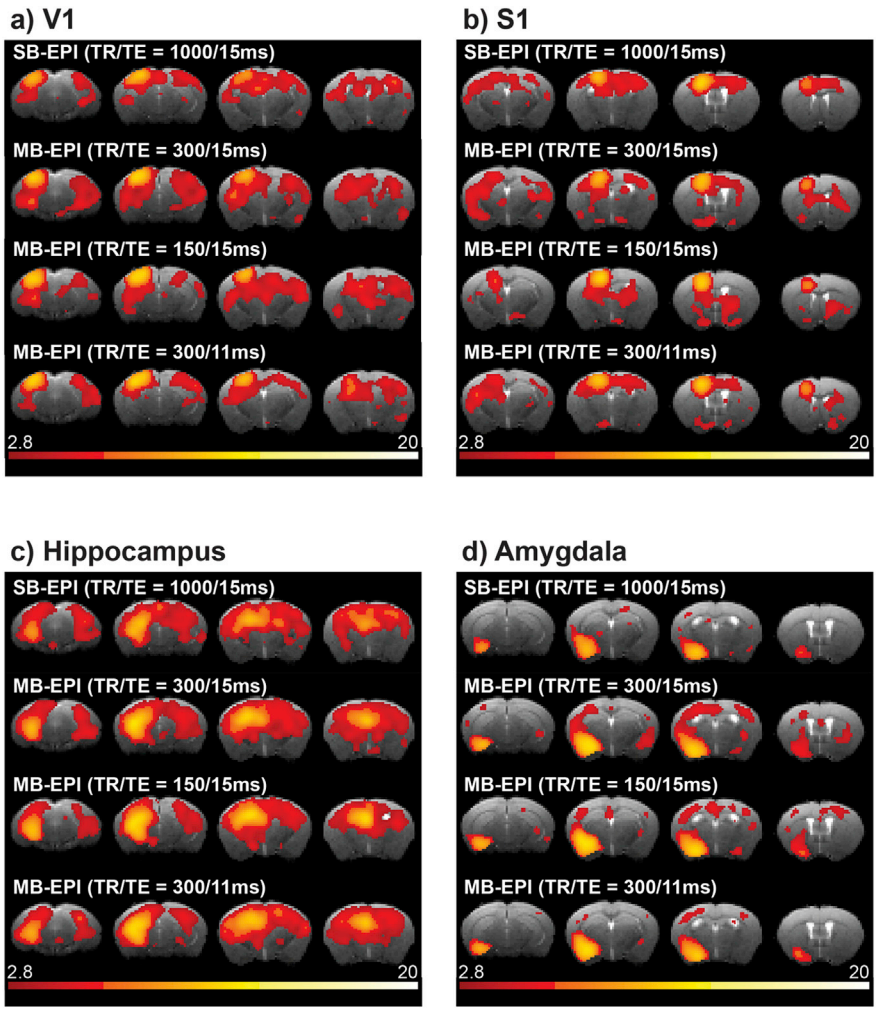

Fig. 6. Resting-state functional connectivity with high-pass filtered at 0.01Hz. Group resting-state functional connectivity maps ($p < 0.05$, FDR corrected, $N = 8$) using seed regions in the right **a)** V1, **b)** S1, **c)** hippocampus, and **d)** amygdala.

4. Discussion

We demonstrated the first practical SMS technique for high temporal resolution fMRI of the rodent brain without the need of a coil array. With extended FOV and phase encoding, 4 slices could be simultaneously acquired with moderate increase of susceptibility artifacts. The MB-EPI significantly shortened the TR for acquiring the whole brain. Particularly, the increased readout length increased SNR, leading to a comparable SNR and tSNR at a TR of 300 ms as the conventional EPI at TR = 1000 ms. These together resulted in drastically increased sensitivity to functional activation due to the increased sampling rate. By reducing the number of slices to cover only the whole cerebrum, fMRI as fast as 150 ms was achieved with similar functional sensitivity as TR = 300 ms. Compared to currently used line-scanning method for ultrafast fMRI in rodents (Silva and Koretsky, 2002; Albers et al., 2018), the MB-EPI provides whole brain coverage instead of just 1D information per TR and hence enables investigating neural dynamics and interactions across the brain. It should be noted that the same MB-EPI protocol could be easily adapted to rat fMRI using larger FOV and thicker slice.

Although reducing the matrix size to acquire a rectangle FOV that covers only the brain could also reduce the scan time, this leads to a lower SNR due to the reduced k-space sampling (e.g, >40% reduction if only half FOV is acquired). On the contrary, the proposed multiband acquisition could generate higher tSNR compared to SB-EPI with the same TR/TE and volume coverage. This is mainly because of the 2× longer readout window for full k-space, which ideally results in 44% higher SNR, and 1.5-fold for ¾ partial Fourier acquisition, which ideally leads to 84% higher SNR. Although the SNR gain should be slightly lower than the theoretical estimate due to the T_2^* decay over the EPI echo train, the spatial SNR measured in the phantom was only comparable to the SB-EPI. This is likely due to the increased susceptibility artifacts and residual ghosts from other slices. However, tSNR gain was in line with the theoretic estimate. Therefore the tSNR gain can be traded for higher spatial and/or temporal resolutions. As demonstrated in the TR = 300 ms scans, both spatial and temporal SNR were only reduced slightly due to the decreased T_1 recovery.

The substantially increased number of time points (3.3× for TR = 300 ms and 6.7× for TR = 150 ms) for the same scan duration could drastically increase the detection power in an fMRI experiment. Our results show an average of 77% increase of z-score and more than 4 times increase of activated pixel number in the visual cortex using a visual stimulation, which is consistent with the theoretically estimated increase of 87% (= 1.2 signal change × 0.86 tSNR × $\sqrt{3.3}$ scan number). Another factor that may contribute to the sensitivity improvement is the separation of physiological artifacts. The mouse respiration rate in this study ranged roughly between 1.9 and 2.4 Hz. It would be aliased to 0–0.4 Hz and overlapped with the task frequency (~0.017 Hz) at TR = 1000 ms and hence interfere with the detection of task activation using SB-EPI. With the high frame rate of 3.3 Hz, the respiration would be aliased to a higher frequency range (0.9–1.4 Hz) that is away from the task activation. In-flow effect may also enhancement the signal change at shorter TR, though the use of Ernst angle would reduce its contribution. The

increased statistical power will benefit the detection of activation in rodents, particularly the mouse which has been previously shown to have very low signal change in the visual cortex (Niranjan et al., 2016), auditory pathway (Freches et al., 2018) and somatosensory cortex (Nasrallah et al., 2014; Chang et al., 2018). With the sensitivity enhancement and separation of physiological artifacts by the MB-EPI, clear visual activation can also be detected even with a TR as short as 150 ms.

Compared to TR = 300 ms, the reduction of tSNR at TR = 150 ms could be largely compensated by the 2× increase of temporal samples. However, the detected activated area was still smaller. The slightly lower sensitivity may be because the actual HRF became critical in data analysis at such high temporal resolution. Early study had reported fast BOLD HRF in the rat brain with a time-to-peak around 2s (Silva et al., 2007). Recently, a study comparing the influence of different anesthesia on the HRF in the mouse brain showed complicated dynamics that may not be modeled well using typical gamma variate functions (Schlegel et al., 2015). Besides, the temporal autocorrelation is expected to be higher at sub-second temporal resolution, which would lead to increased false positive using typical autoregressive (AR) model of the 1st order (Bollmann et al., 2018). As the FSL FILM uses an adaptive approach to estimate and reduce autocorrelation, it may be suitable for analyzing ultrafast fMRI data (Demetriou et al., 2018). Further study would be needed to determine an appropriate HRF under the particular anesthetic setting and to evaluate the influence of noise model for ultrahigh temporal resolution imaging. The high temporal resolution of MB-EPI would allow more precise estimation of HRF in this regard.

Previous studies in human have suggested that ultrafast imaging could improve the detection of transient neural dynamics, dynamic connectivity while separating non-neural fluctuations that are faster than BOLD (for review, see LeVan et al., 2018). Studies in human have demonstrated improved statistic power and specificity in task fMRI using sub-second temporal resolution (Chen et al., 2015; Demetriou et al., 2018; Yoo et al., 2018), which is consistent with what we found in the mouse brain. With the high-speed MB-EPI, it will allow the use of sparse temporal sampling for studying auditory activation (Freches et al., 2018), or to compare fMRI time-series with optical measurement which has very high sampling rate (Sanganahalli et al., 2016).

Unlike the results of task fMRI, no significant difference was found between the protocols in the resting-state functional connectivity. As the connectivity strength should not change with temporal resolution unless the noise starts to dominate, it is not surprising to see comparable inter-regional correlation. Comparing the results with or without lowpass filtering, the inclusion of high frequency component in resting fMRI reduced the connectivity z-score but did not change the connectivity pattern, except for the amygdala network. The increased sensitivity of the MB-EPI with TR/TE = 300/15 ms enhanced the detection of bilateral amygdala connectivity. Furthermore, bandpass filtering allowed clear detection of amygdala-striatal connectivity, which may be due to the reduction of physiological artifacts that were aliased to above 1 Hz in MB-EPI. Recent studies in human also showed that ultrafast imaging could improve the separation of noise component and slightly increased top range z-score, but the identified networks were comparable with those of a typical TR unless short duration was used (Demetriou et al., 2018; Jahanian et al., 2019). Therefore, the advantage of ultrafast imaging for resting fMRI analysis would be to study the dynamic changes over short time windows (Sahib et al., 2018).

With the reduced scan time, it is possible to increase spatial resolution using the MB-EPI. To evaluate the feasibility, a high spatial resolution ($0.15 \times 0.15 \times 0.6\,mm^3$) fMRI was conducted using a MB factor of 2 to acquire 14 slices with TR/TE = 500/15 ms. Our preliminary results show that visual activation could be detected during a 6-min paradigm consisting of five alternated resting and stimulation blocks (Supplementary Fig. S3a). However, the tSNR of the high-resolution MB-EPI was only about 25% of the SB-EPI with $0.3 \times 0.3\,mm^2$ in-plane resolution. More data averaging will be needed to compensate the highly reduced tSNR. Besides, as the longer echo train increases the broadening of PSF along the phase encoding direction, the resulted pixel blurring limits further increase of spatial resolution. Therefore multi-shot acquisition is still preferable for high resolution imaging. The shortened TR using MB-EPI could allow multi-shot imaging without much sacrifice of temporal resolution.

Another way to increase spatial resolution is to acquire thinner slices. We performed a 4-band EPI to acquire 36 thin slices of 0.25 mm (gap = 0.05 mm) with in-plane resolution of 0.3 mm and TR/TE = 500/15 ms. Despite a 2× reduction of SNR, visual activation could also be detected using a 6-min paradigm (Supplementary Fig. S3b). An advantage of using thin slices is the reduction of susceptibility artifact as the through-slice dephasing would be much less. Compared to the images of 0.5 mm slice thickness, the percentage difference map (Supplementary Fig. S3b, bottom row) showed less signal drop-out around the lower edge of the brain, which is closer to the ear canals. Therefore, besides increasing temporal resolution, one could also use MB-EPI to increase either in-plane or through-plane resolution while achieving sub-second TR for high spatiotemporal resolution imaging.

The prolonged TE and readout window of the MB-EPI method leads to more signal decay, susceptibility artifacts and distortion. Larger difference between multiband and single-band images can be found near the areas with strong susceptibility. A 3/4 partial Fourier MB-EPI with shorter readout window can reduce this discrepancy as shown in Fig. 2. A shorter TE also helps recover the decayed signal. By reducing the TE from 15 ms to 11 ms, the activation signal change, z-score and area size were slightly reduced, but the z-score and area size were still significantly better than using the SB-EPI. Alternatively, the distortion could be reduced using reverse-phased EPI (Hong et al., 2015). The longer echo train may limit the amount of acceleration when using this sequence at even higher magnetic field like 15.2T where the T_2* is much shorter. To control the susceptibility artifact at such ultrahigh field, a smaller MB factor of 2 could be a more preferable choice. Alternatively, multi-dimensional spectral-spatial RF pulse shaping strategies could be used to reduce the B_0 distortion of the excitation profile (Stenger et al., 2000; Dumez and Frydman, 2013). Power scaling methods like variable rate excitation (Conolly et al., 1988) or power independent of the number of slices (Norris et al., 2011; Koopmans et al., 2013) could be used to reduce RF power demand at higher fields. For further acceleration, array coil with multiple elements along the slice direction would be needed to allow slice overlap so that echo train does not need to be increased that much. A stronger gradient system with higher slew rate will also effectively shorten the EPI readout length to reduce susceptibility artifact, or allow the acquisition of full k-space to reduce blurring in the phase-encoding direction. On the other hand, the MB-EPI is expected to have better image quality at lower magnetic field like 7T with longer T_2* and smaller magnetic field inhomogeneity.

The ghost artifacts from other slices caused by the G_z blips were in the order of 5%. No significant slice aliasing was found that affected the detection of task activation and functional connectivity. However, the leaked signal would be stronger when using more sensitive coils (like cryoprobe) or at much higher magnetic field and hence may lead to false positive. Recent studies on SMS-EPI in human fMRI also show significant slice leakage artifacts, which could be reduced by a slice-GRAPPA method that takes such artifacts into account (Risk et al., 2018). Further improving the ghost correction and reconstruction kernel may be needed to further suppressing such slice leakage artifact in the MB-EPI.

5. Conclusion

We successfully demonstrated a SMS EPI for ultrafast fMRI of the mouse brain on a pre-clinical scanner without the use of receiving coil array. With a MB factor of 4, a temporal resolution of 300 ms could be easily achieved while maintaining the same spatial resolution and whole brain coverage. The TR can be further pushed to 150 ms with typical slice number used in many rodent fMRI studies. The increased speed can be

used to attain higher degrees of freedom for the fMRI time-series analysis, distinguish transient and detailed hemodynamic changes, or to further increase the in-plane or through-plane spatial resolution for high spatiotemporal resolution imaging. Such ultrafast fMRI will allow detecting fast neural dynamics in task and resting state to understand their neural mechanisms in animal models. As MB-EPI has been shown to beneficial to arterial spin labeling perfusion imaging with a reduction of arterial transit time difference between slices (Kim et al., 2013), this method could be combined with spin labeling to improve perfusion imaging quality. With further design of multiband refocusing pulses, this method could also be extended to spin-echo EPI for reducing susceptibility artifacts in fMRI or accelerating diffusion tensor imaging.

Acknowledgement

We thank Dr Yunpeng Wang for his kind support on the *in vivo* data collection. The study was funded by the Queensland Brain Institute and Centre for Advanced Imaging, The University of Queensland, and by the Mason Foundation grant #MAS2017F031, Australia.

Appendix A. Supplementary data

Supplementary data to this article can be found online at https://doi.org/10.1016/j.neuroimage.2019.03.045.

References

Albers, F., Schmid, F., Wachsmuth, L., Faber, C., 2018. Line scanning fMRI reveals earlier onset of optogenetically evoked BOLD response in rat somatosensory cortex as compared to sensory stimulation. Neuroimage 164, 144–154.
Bollmann, S., Puckett, A.M., Cunnington, R., Barth, M., 2018. Serial correlations in single-subject fMRI with sub-second TR. Neuroimage 166, 152–166.
Boubela, R.N., Kalcher, K., Huf, W., Kronnerwetter, C., Filzmoser, P., Moser, E., 2013. Beyond noise: using temporal ICA to extract meaningful information from high-frequency fMRI signal fluctuations during rest. Front. Hum. Neurosci. 7, 168.
Chang, W.-T., Puspitasari, F., Garcia-Miralles, M., Yeow, L.Y., Tay, H.-C., Koh, K.B., Tan, L.J., Pouladi, M.A., Chuang, K.-H., 2018. Connectomic imaging reveals Huntington-related pathological and pharmaceutical effects in a mouse model. NMR Biomed. 31, e4007.
Chen, J.E., Glover, G.H., 2015. BOLD fractional contribution to resting-state functional connectivity above 0.1 Hz. Neuroimage 107 (C), 207–218.
Chen, L., Vu, A.T., Xu, J., Moeller, S., Ugurbil, K., Yacoub, E., Feinberg, D.A., 2015. Evaluation of highly accelerated simultaneous multi-slice EPI for fMRI. Neuroimage 104, 452–459.
Chou, N., Wu, J., Bai, B.J., Qiu, A., Chuang, K.-H., 2011. Robust automatic rodent brain extraction using 3-D pulse-coupled neural networks (PCNN). IEEE Trans Image Process 20 (9), 2554-64.
Chuang, K.H., Chen, J.H., 2001. IMPACT: image-based physiological artifacts estimation and correction technique for functional MRI. Magn. Reson. Med. 46 (2), 344–353.
Chuang, K.H., Lee, H.L., Li, Z., Chang, W.T., Nasrallah, F.A., Yeow, L.Y., Singh, K.K.D./O.R., 2019. Evaluation of nuisance removal for functional MRI of rodent brain. Neuroimage 188, 694–709.
Chuang, K.-H., Nasrallah, F.A., 2017. Functional networks and network perturbations in rodents. Neuroimage 163, 419–436.
Conolly, S., Nishimura, D., Macovski, A., Glover, G., 1988. Variable-rate selective excitation. J. Magn. Reson. 78, 440–458.
de Graaf, R.A., Brown, P.B., McIntyre, S., Nixon, T.W., Behar, K.L., Rothman, D.L., 2006. High magnetic field water and metabolite protonT1 andT2 relaxation in rat brain in vivo. Magn. Reson. Med. 56 (2), 386–394.
Demetriou, L., Kowalczyk, O.S., Tyson, G., Bello, T., Newbould, R.D., Wall, M.B., 2018. A comprehensive evaluation of increasing temporal resolution with multiband-accelerated protocols and effects on statistical outcome measures in fMRI. Neuroimage 176, 404–416.
Dumez, J.-N., Frydman, L., 2013. Multidimensional excitation pulses based on spatiotemporal encoding concepts. J. Magn. Reson. 226, 22–34.
Duong, T.Q., Kim, D.S., Ugurbil, K., Kim, S.G., 2001. Localized cerebral blood flow response at submillimeter columnar resolution. Proc. Natl. Acad. Sci. U. S. A 98, 10904–10909.
Feinberg, D.A., Yacoub, E., 2012. The rapid development of high speed, resolution and precision in fMRI. Neuroimage 62, 720–725.
Feinberg, D.A., Moeller, S., Smith, S.M., 2010. Multiplexed echo planar imaging for sub-second whole brain FMRI and fast diffusion imaging. PLoS One 5, e15710.
Frahm, J., Merboldt, K.D., Hanicke, W., 1993. Functional MRI of human brain activation at high spatial resolution. Magn. Reson. Med. 29 (1), 139–144.
Freches, G.B., Chavarrias, C., Shemesh, N., 2018. BOLD-fMRI in the mouse auditory pathway. Neuroimage 165, 265–277.
Glover, G.H., 1991. Phase-offset multiplanar (POMP) volume imaging: a new technique. J. Magn. Reson. Imaging 1 (4), 457–461.
Goense, J., Bohraus, Y., Logothetis, N.K., 2016. fMRI at high spatial resolution: implications for BOLD-models. Front. Comput. Neurosci. 10, 232-13.
Griswold, M.A., Jakob, P.M., Heidemann, R.M., Nittka, M., Jellus, V., Wang, J., Kiefer, B., Haase, A., 2002. Generalized autocalibrating partially parallel acquisitions (GRAPPA). Magn. Reson. Med. 47 (6), 1202–1210.
Guilfoyle, D.N., Dyakin, V.V., O'Shea, J., Pell, G.S., Helpern, J.A., 2003. Quantitative measurements of proton spin-lattice (T1) and spin-spin (T2) relaxation times in the mouse brain at 7.0 T. Magn. Reson. Med. 49 (3), 576–580.
Harel, N., Lin, J., Moeller, S., Ugurbil, K., Yacoub, E., 2006. Combined imaging-histological study of cortical laminar specificity of fMRI signals. Neuroimage 29, 879–887.
Hennig, J., Zhong, K., Speck, O., 2007. MR-encephalography: fast multi-channel monitoring of brain physiology with magnetic resonance. Neuroimage 34, 212–219.
Hong, X., To, X.V., Teh, I., Soh, J.R., Chuang, K.-H., 2015. Evaluation of EPI distortion correction methods for quantitative MRI of the brain at high magnetic field. Magn. Reson. Imaging 33, 1098–1105.
Huber, L., Handwerker, D.A., Jangraw, D.C., Chen, G., Hall, A., Stüber, C., Gonzalez-Castillo, J., Ivanov, D., Marrett, S., Guidi, M., Goense, J., Poser, B.A., Bandettini, P.A., 2017. High-resolution CBV-fMRI allows mapping of laminar activity and connectivity of cortical input and output in human M1. Neuron 96 (6), 1253–1257.
Jahanian, H., Holdsworth, S., Christen, T., Wu, H., Zhu, K., Kerr, A.B., Middione, M.J., Dougherty, R.F., Moseley, M., Zaharchuk, G., 2019. Advantages of short repetition time resting-state functional MRI enabled by simultaneous multi-slice imaging. J. Neurosci. Methods 311, 122–132.
Kim, T., Shin, W., Zhao, T., Beall, E.B., Lowe, M.J., Bae, K.T., 2013. Whole brain perfusion measurements using arterial spin labeling with multiband acquisition. Magn. Reson. Med. 70, 1653–1661.
Koopmans, P.J., Boyacioglu, R., Barth, M., Norris, D.G., 2013. Simultaneous multislice inversion contrast imaging using power independent of the number of slices (PINS) and delays alternating with nutation for tailored excitation (DANTE) radio frequency pulses. Magn. Reson. Med. 69, 1670–1676.
Lan, P., Islam, H., Glover, G., 2017. Phase-offset multiplanar echo-planar imaging (POMP-EPI) to accelerate fMRI acquisition without parallel imaging. Proc. ISMRM 2017, 1632.
Lee, H.-L., Zahneisen, B., Hugger, T., LeVan, P., Hennig, J., 2013. Tracking dynamic resting-state networks at higher frequencies using MR-encephalography. Neuroimage 65 (C), 216–222.
LeVan, P., Akin, B., Hennig, J., 2018. Fast imaging for mapping dynamic networks. Neuroimage 180, 547–558.
Lewis, L.D., Setsompop, K., Rosen, B.R., Polimeni, J.R., 2016. Fast fMRI can detect oscillatory neural activity in humans. Proc. Natl. Acad. Sci. U. S. A 113 (43), E6679–E6685.
Lin, F.-H., Chu, Y.-H., Hsu, Y.-C., Lin, J.-F., Tsai, W.-K., Tsai, S.-Y., Kuo, W.-J., 2015. Significant feed-forward connectivity revealed by high frequency components of BOLD fMRI signals. Neuroimage 121 (C), 69–77.
Maudsley, A.A., 1980. Multiple-line-scanning spin-density imaging. J. Magn. Reson. 41, 112–126.
Moeller, S., Yacoub, E., Olman, C.A., Auerbach, E., Strupp, J., Harel, N., Ugurbil, K., 2010. Multiband multislice GE-EPI at 7 Tesla, with 16-fold acceleration using partial parallel imaging with application to high spatial and temporal whole-brain fMRI. Magn. Reson. Med. 63, 1144–1153.
Müller, S., 1988. Multifrequency selective RF pulses for multislice MR imaging. Magn. Reson. Med. 6, 364–371.
Nasrallah, F.A., Tay, H., Chuang, K.-H., 2014. Detection of functional connectivity in the resting mouse brain. Neuroimage 86, 417–424.
Neggers, S.F., Hermans, E.J., Ramsey, N.F., 2008. Enhanced sensitivity with fast three-dimensional blood-oxygen-level-dependent functional MRI: comparison of SENSE-PRESTO and 2D-EPI at 3 T. NMR Biomed. 21, 663–676.
Niranjan, A., Christie, I.N., Solomon, S.G., Wells, J.A., Lythgoe, M.F., 2016. fMRI mapping of the visual system in the mouse brain with interleaved snapshot GE-EPI. Neuroimage 139, 337–345.
Norris, D.G., Koopmans, P.J., Boyacioglu, R., Barth, M., 2011. Power Independent of Number of Slices (PINS) radiofrequency pulses for low-power simultaneous multislice excitation. Magn. Reson. Med. 66, 1234–1240.
Pohmann, R., Shajan, G., Balla, D.Z., 2011. Contrast at high field: relaxation times, magnetization transfer and phase in the rat brain at 16.4 T. Magn. Reson. Med. 66 (6), 1572–1581.
Poplawsky, A.J., Fukuda, M., Murphy, M., Kim, S.G., 2015. Layer-specific fMRI responses to excitatory and inhibitory neuronal activities in the olfactory bulb. J. Neurosci. 35 (46), 15263–15275.
Posse, S., Ackley, E., Mutihac, R., Rick, J., Shane, M., Murray-Krezan, C., Zaitsev, M., Speck, O., 2012. Enhancement of temporal resolution and BOLD sensitivity in real-time fMRI using multi-slab echo-volumar imaging. Neuroimage 61, 115–130.
Pruessmann, K.P., Weiger, M., Scheidegger, M.B., Boesiger, P., 1999. SENSE: sensitivity encoding for fast MRI. Magn. Reson. Med. 42 (5), 952–962.
Risk, B.B., Kociuba, M.C., Rowe, D.B., 2018. Impacts of simultaneous multislice acquisition on sensitivity and specificity in fMRI. Neuroimage 172, 538–553.
Sahib, A.K., Erb, M., Marquetand, J., Martin, P., Elshahabi, A., Klamer, S., Vulliemoz, S., Scheffler, K., Ethofer, T., Focke, N.K., 2018. Evaluating the impact of fast-fMRI on dynamic functional connectivity in an event-based paradigm. PLoS One 13, e0190480.
Sanganahalli, B.G., Rebello, M.R., Herman, P., Papademetris, X., Shepherd, G.M., Verhagen, J.V., Hyder, F., 2016. Comparison of glomerular activity patterns by fMRI and wide-field calcium imaging: implications for principles underlying odor mapping. Neuroimage 126, 208–218.

Schlegel, F., Schroeter, A., Rudin, M., 2015. The hemodynamic response to somatosensory stimulation in mice depends on the anesthetic used: implications on analysis of mouse fMRI data. Neuroimage 116, 40–49.

Setsompop, K., Gagoski, B.A., Polimeni, J.R., Witzel, T., Wedeen, V.J., Wald, L.L., 2012. Blipped-controlled aliasing in parallel imaging for simultaneous multislice echo planar imaging with reduced g-factor penalty. Magn. Reson. Med. 67, 1210–1224.

Siero, J.C., Petridou, N., Hoogduin, H., Luijten, P.R., Ramsey, N.F., 2011. Cortical depth-dependent temporal dynamics of the BOLD response in the human brain. J. Cereb. Blood Flow Metab. 31, 1999–2008.

Silva, A.C., Koretsky, A.P., 2002. Laminar specificity of functional MRI onset times during somatosensory stimulation in rat. Proc. Natl. Acad. Sci. U.S.A. 99 (23), 15182–15187.

Silva, A.C., Koretsky, A.P., Duyn, J.H., 2007. Functional MRI impulse response for BOLD and CBV contrast in rat somatosensory cortex. Magn. Reson. Med. 57, 1110–1118.

Smith, S.M., Beckmann, C.F., Andersson, J., Auerbach, E.J., Bijsterbosch, J., Douaud, G., Duff, E., Feinberg, D.A., Griffanti, L., Harms, M.P., Kelly, M., Laumann, T., Miller, K.L., Moeller, S., Petersen, S., Power, J., Salimi-Khorshidi, G., Snyder, A.Z., Vu, A.T., Woolrich, M.W., Xu, J., Yacoub, E., Ugurbil, K., Van Essen, D.C., Glasser, M.F., Consortium, W.U.-M.H., 2013. Resting-state fMRI in the human connectome project. Neuroimage 80, 144–168.

Souza, S.P., Szumowski, J., Dumoulin, C.L., Plewes, D.P., Glover, G., 1988. SIMA - simultaneous multislice acquisition of MR images by Hadamard-encoded excitation. J. Comput. Assist. Tomogr. 12, 1026–1030.

Stenger, V.A., Boada, F.E., Noll, D.C., 2000. Three-dimensional tailored RF pulses for the reduction of susceptibility artifacts in T_2*-weighted functional MRI. Magn. Reson. Med. 44, 525–531.

Tong, Y., Hocke, L.M., Frederick, B., 2014. Short repetition time multiband echo-planar imaging with simultaneous pulse recording allows dynamic imaging of the cardiac pulsation signal. Magn. Reson. Med. 72, 1268–1276.

Ullmann, J.F.P., Watson, C., Janke, A.L., Kurniawan, N.D., Reutens, D.C., 2013. A segmentation protocol and MRI atlas of the C57BL/6J mouse neocortex. Neuroimage 78 (C), 196–203.

Yoo, P.E., John, S.E., Farquharson, S., Cleary, J.O., Wong, Y.T., Ng, A., Mulcahy, C.B., Grayden, D.B., Ordidge, R.J., Opie, N.L., O'Brien, T.J., Oxley, T.J., Moffat, B.A., 2018. 7T-fMRI: faster temporal resolution yields optimal BOLD sensitivity for functional network imaging specifically at high spatial resolution. Neuroimage 164, 214–229.

Zhao, F., Wang, P., Kim, S.-G., 2004. Cortical Depth-Dependent Gradient-Echo and Spin-Echo BOLD fMRI at 9.4T. Magn. Reson. Med 51, 518–524.